

Article

Characterization of Lithium-Ion Battery Fire Emissions—Part 1: Chemical Composition of Fine Particles (PM_{2.5})

Matthew Claassen ^{1,2}, Bjoern Bingham ^{1,3}, Judith C. Chow ¹, John G. Watson ¹ , Yan Wang ²  and Xiaoliang Wang ^{1,*} 

¹ Division of Atmospheric Sciences, Desert Research Institute, Reno, NV 89512, USA; matt.claassen@dri.edu (M.C.); bjoern.bingham@dri.edu (B.B.); judy.chow@dri.edu (J.C.C.); john.watson@dri.edu (J.G.W.)

² Department of Mechanical Engineering, University of Nevada, Reno, NV 89557, USA; yanwang@unr.edu

³ Atmospheric Sciences, Department of Physics, University of Nevada, Reno, NV 89557, USA

* Correspondence: xiaoliang.wang@dri.edu; Tel.: +1-775-674-7177

Abstract: Lithium-ion batteries (LIB) pose a safety risk due to their high specific energy density and toxic ingredients. Fire caused by LIB thermal runaway (TR) can be catastrophic within enclosed spaces where emission ventilation or occupant evacuation is challenging or impossible. The fine smoke particles (PM_{2.5}) produced during a fire can deposit in deep parts of the lung and trigger various adverse health effects. This study characterizes the chemical composition of PM_{2.5} released from TR-driven combustion of cylindrical lithium iron phosphate (LFP) and pouch-style lithium cobalt oxide (LCO) LIB cells. Emissions from cell venting and flaming combustion were measured in real time and captured by filter assemblies for subsequent analyses of organic and elemental carbon (OC and EC), elements, and water-soluble ions. The most abundant PM_{2.5} constituents were OC, EC, phosphate (PO₄³⁻), and fluoride (F⁻), contributing 7–91%, 0.2–40%, 1–44%, and 0.7–3% to the PM_{2.5} mass, respectively. While OC was more abundant during cell venting, EC and PO₄³⁻ were more abundant when flaming combustion occurred. These freshly emitted particles were acidic. Overall, particles from LFP tests had higher OM but lower EC compared to LCO tests, consistent with the higher thermal stability of LFP cells.



Citation: Claassen, M.; Bingham, B.; Chow, J.C.; Watson, J.G.; Wang, Y.; Wang, X. Characterization of Lithium-Ion Battery Fire Emissions—Part 1: Chemical Composition of Fine Particles (PM_{2.5}). *Batteries* **2024**, *10*, 301. <https://doi.org/10.3390/batteries10090301>

Academic Editor: Wojciech Mrozek

Received: 27 June 2024

Revised: 6 August 2024

Accepted: 20 August 2024

Published: 27 August 2024



Copyright: © 2024 by the authors. Licensee MDPI, Basel, Switzerland. This article is an open access article distributed under the terms and conditions of the Creative Commons Attribution (CC BY) license (<https://creativecommons.org/licenses/by/4.0/>).

1. Introduction

Lithium-ion batteries (LIB) are a ubiquitous component in modern consumer products and commercial systems. Fire safety is a critical concern for LIBs due to their high energy densities [1,2]. Failing LIBs possess all three components needed for a fire (i.e., fuel, oxygen, and heat) in close contact, thereby allowing combustion to occur even when deprived of ambient air [1]. LIB electrolytes, separator and binder materials, and anodes are all combustible under suitable conditions. Oxygen can be released from cathode decomposition or is available from ambient air once the cell casing is compromised. Heat can be generated internally from a short-circuit or from exothermic chemical reactions, both of which occur during initial cell breakdown. Heat can also be applied externally by fire, neighboring cell failure, or other overheating components. As a result, when LIBs overheat, are used improperly, or are defective, they can enter an exothermic chain reaction known as thermal runaway (TR), which may further lead to violent combustion and even explosion.

Numerous fire incidents have been reported for LIBs of various sizes and in different applications. Between the years 2010 and July 2023, 393 electrical vehicle (EV) fire incidents were reported globally, most of them occurring after 2020 due to increasing EV prevalence [3]. Several large fires have occurred at stationary storage facilities. The 250 MW Gateway Energy Storage facility fire in San Diego, California, burned for over a week in 2024. The fire risk and consequences for light EVs (e.g., electric scooters and bikes) are

much higher than those for passenger EVs owing to lower quality LIB cells and battery management systems, device wear and tear, and variable domestic charging methods. Over 500 LIB fires, resulting in 36 fatalities, were caused by light EVs between January and July 2023 alone [3]. LIBs also pose risks to transportation. The Federal Aviation Administration (FAA) has recorded over 250 incidents of smoke, fire, extreme heat, or explosion involving LIBs aboard aircraft in the last 10 years. Three incidences suspected of being caused by LIBs carried as cargo resulted in the loss of the aircraft and crew [4]. While a major LIB fire has not yet occurred during a manned space mission, NASA test centers have experienced catastrophic LIB failures, even in advanced, custom-designed applications that had seen prolonged use without incident [5]. Fire risks persist even at the end of a LIB's useful life [6]. The U.S. Environmental Protection Agency (U.S. EPA) found that 245 fires across 64 waste facilities in the U.S. were definitely or probably caused by lithium (Li) metal, or LIBs, between the years 2013 and 2020 [7].

In addition to intense heat and flame, LIB fires can generate large quantities of combustible, toxic, and corrosive gaseous and particulate emissions. Past studies on LIB fire emissions focus on combustible and/or toxic gaseous compounds [8–16]. Fewer studies have examined smoke particle emissions from LIB fires [17–23]. Several studies measured the elemental composition of large particles (up to several millimeters in diameter) deposited on nearby surfaces after a LIB fire and found that these particles are enriched with toxic and corrosive chemicals, including Li, transition metals, fluoride compounds, and carbonates [17,20,21,24]. However, many of these elemental measurements used scanning electron microscopy-energy dispersive X-ray analysis (SEM-EDX) under vacuum conditions, causing volatile particulate compounds to evaporate. Therefore, the volatile compounds are not reported. While these large particles ($>100\text{ }\mu\text{m}$) may cause soil and water contamination, they settle out quickly and are not likely to penetrate deep into the human respiratory track.

Very few studies have examined the smaller particles ($<10\text{ }\mu\text{m}$) that pose significant inhalation hazards. Barone et al. [18] pointed out that little information was available on the size, composition, and morphology of respirable particles. They used image and elemental analyses of particles from the combustion of three types of LIBs: nickel manganese cobalt oxide (NMC), lithium iron phosphate (LFP), and lithium titanate oxide (LTO) and found abundant elements originating from LIB anode, cathode, and separator materials. NMC and LTO particles had higher abundances of transition metals (e.g., nickel [Ni], manganese [Mn], cobalt [Co], and titanium [Ti]) than LFP particles, causing greater health and environmental contamination concerns. However, that study did not report particle concentrations, and the composition focused mostly on elements that can be analyzed by EDX. Premnath et al. [19] measured total and solid PM_{2.5} (particles with aerodynamic diameters $\leq 2.5\text{ }\mu\text{m}$) concentrations, black carbon levels, and organic and elemental carbon (OC and EC) for NMC and LFP cells at 100% state of charge (SOC). OC and EC were 17–47% and 7–33% of PM_{2.5}, respectively; however, elements and ions were not measured. Padilla et al. [22] showed high smoke concentrations and obscurations from laptop computer fires, highlighting the potential catastrophic hazards of LIB fires in spacecraft. Xu et al. [25,26] characterized the morphology, elemental composition, surface chemistry, and cytotoxicity of soot collected from combusting LFP and ternary cells. Particles were collected inside or close to the flame without size classification. To the best of our knowledge, no studies have reported the detailed chemical composition of PM_{2.5} from LIB fires.

The objectives of this paper are to: (1) determine the chemical composition of PM_{2.5} emitted from LIB combustion events; and (2) evaluate the dependence of PM_{2.5} compositions on cell chemistry and SOC. The PM_{2.5} size fraction of particles from LIB fires is of particular concern in terms of human health. While larger particles quickly settle on surrounding surfaces due to gravity, PM_{2.5} can stay airborne much longer; when inhaled, these particles can penetrate deep into the lung [27]. Toxic constituents of PM_{2.5} can either accumulate in the lung or enter the bloodstream, leading to respiratory, cardiovascular, and other diseases [28]. Depending on exposure level and individual susceptibility, PM_{2.5} can

cause both acute and chronic health effects. A recent study by Xu et al. found that soot particles from LIB fires have significant cytotoxicity to human cells, causing greater damage than smoke particles from wood combustion [26]. In addition, the chemical characteristics of emitted PM_{2.5} are useful for fire detection, personal protection, fire suppression, and postfire cleanup. A companion paper [29] presents particle size distributions and emission factors, and a future paper will describe toxic, combustible, and corrosive gas emissions.

2. Materials and Methods

2.1. Tested LIBs

LIBs are often categorized by their cathode composition. Two commonly used cathode types (i.e., “cell chemistries”) were tested: a cylindrical, 18650-style, LFP cell manufactured by LithiumWerks (Enschede, The Netherlands), and a pouch-style lithium cobalt oxide (LCO) cell manufactured by AA Portable Power Corp. (Richmond, CA, USA) (as shown in Figure S1 of Supplementary Materials). These cells were commercially available and were safe to handle, charge, and discharge with minimal specialty equipment. The cells were purchased shortly before testing and were received at proper storage voltages. Specifications for each LIB type are shown in Table 1.

Table 1. Specifications for the two cell types tested [30,31].

Cell Type	Cell Format	Cathode Chemistry	Dimensions (mm)	Nominal Voltage (V)	Nominal Capacity (Ah)	Average Cell Mass (g)
LFP	Cylinder	LiFePO ₄	18 × 18 × 65	3.3	1.1	42
LCO	Pouch	LiCoO ₂	5.4 × 47 × 95	3.7	2.5	47

Cell chemistry can affect the combustion behavior of a compromised LIB cell. As illustrated in Figure S2, LFP cells have increased thermal stability and reduced heat generation during cell breakdown [32–35], but they are disadvantaged by having a lower energy density. LCO cells are the least thermally stable of common cathode chemistries, but they are commonly manufactured due to their high energy density, discharge voltage, cycling performance, and legacy as the first mass-produced LIB type. LCO cells are mostly used for personal electronics (e.g., phones, laptops, cameras, etc.) and are common in space applications due to their high energy density [36], including use in the primary international space station power storage system [37]. LCO cells were selected for this study due to their wide use in personal electronics and space applications and the possibility of unique emission profiles due to their thermal instability. LFP cells were selected due to their increasing adoption and contrasting thermal stability to LCO cells. NMC and other Ni-based chemistries have been represented in the current literature on TR emissions and are commonly used in power tools, EVs, and other micromobility devices, such as electric bikes and scooters. However, LFP cell prevalence is also increasing in these markets due to lower costs and increased thermal stability.

2.2. Experimental Setup and Procedures

LIB combustion tests were conducted inside a burn chamber at the Desert Research Institute [38]. The chamber is ~8 m³ and is sealed except for an air intake and a flow-controlled exhaust port (Figure 1). At the beginning of each testing day, all instruments were turned on and allowed to warm up before use. Instrument consumables were checked, along with all sample line ducting connections. The clean air dilution flow rate, discussed below, was adjusted and measured. All particle analyzers had zero-calibrations performed daily. Before each test, the chosen LIB cell was charged to the desired SOC by a programmable charger. The cell was then placed in a ceramic crucible heated by an electric hot plate. A type K thermocouple was used to measure the external cell and flame temperatures. For LFP tests, the thermocouple was placed next to the cell overpressure vents on the cylinder endcap, where vented gases exit the failing cell. For LCO tests, the thermocouple was

placed above the flat side of the prone cell (see Figure S1). Filter flow rates were measured for each filter channel, and each instrument was configured for data collection. After completing the test setup, the burn chamber door was closed, filter pumps were turned on, and the hotplate power supply was turned on to begin heating the ceramic crucible containing the LIB cell to 450 °C. Different heating rates did not affect emissions, as thermal runaway will occur independently of heating once it has been triggered [39]. The hotplate was left on until the cell had entered TR, combusted, and ceased emitting particles. The time when each event occurred (power on pumps and the heater, smoke visible, flames visible, and flames ending) was recorded. This approach simulates a TR propagation event where a LIB cell is subject to continual heating due to the failure of adjacent cells in a LIB pack. Such a failure mode is responsible for most emissions from large LIB packs, as the failure of any single cell or group of cells spreads through the entire pack.

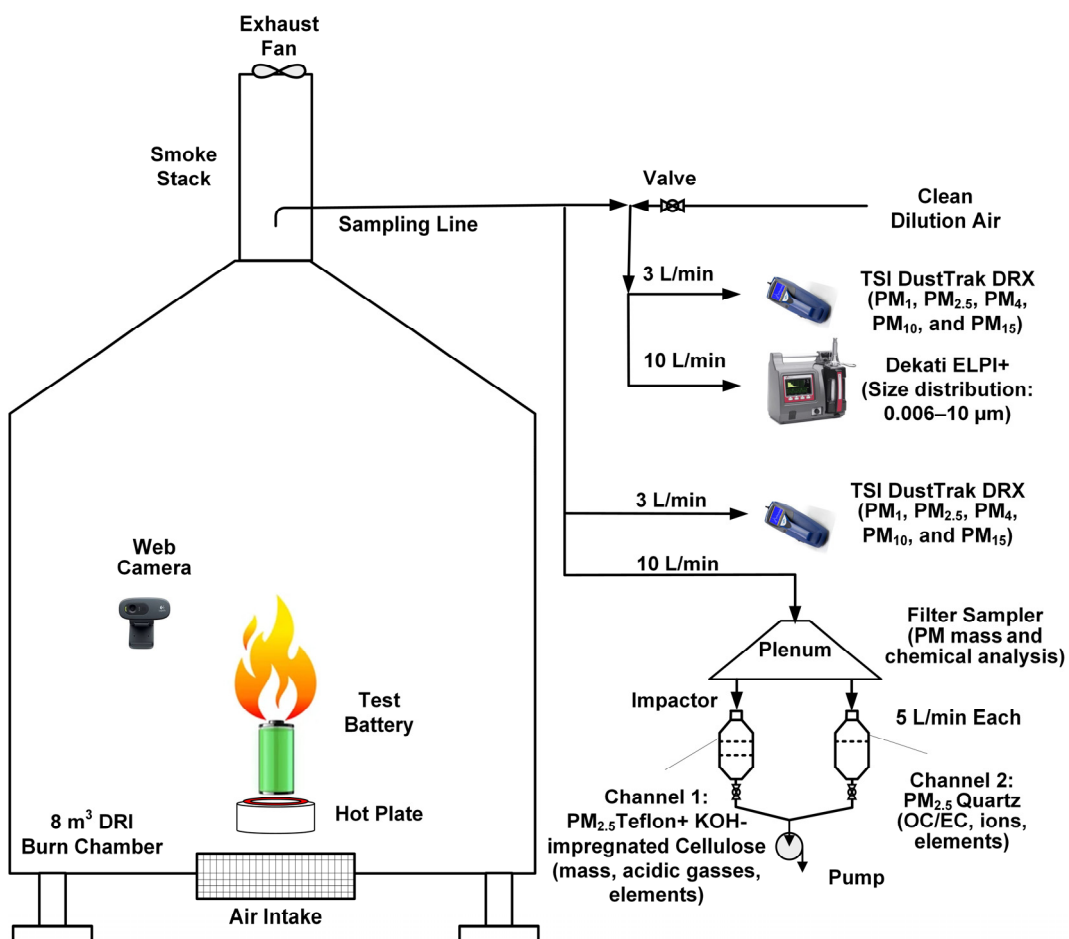


Figure 1. Burn chamber, instrument, and filter assembly layout.

The LIB fire emission sampling setup is similar to that used in previous studies [40–42]. As shown in Figure 1, a sample of LIB combustion emissions was extracted from the exhaust vent and directed to a suite of particle analyzers, as well as the filter sampling system. Particle mass concentrations were measured by two DustTrak DRX (Model 8534, TSI Inc., Shoreview, MN, USA) aerosol monitors in five size fractions (i.e., PM₁, PM_{2.5}, PM₄, PM₁₀, and PM₁₅) [43]. Measurements were made before and after dilution to determine the dilution factors for other instruments. Finer-resolution particle size distributions were measured by an electrical low-pressure impactor (Dekati ELPI+, Kangasala, Finland; 6 nm–10 µm) on the diluted sample line, to prevent impactor overloading [44,45]. Two filter channels with different sampling media were used to collect PM_{2.5} at a flow rate of 5 L/min each and submitted for detailed chemical analyses [46]. Each test started with

a 1–2 min background measurement and ended when particle concentrations returned to background levels after combustion ended. A webcam (Model C270, Logitech, San Jose, CA, USA) was used to record combustion behavior. Gas concentrations were also measured, which will be reported in a future paper.

Each type of LIB was tested at five SOC levels: 0%, 30%, 50%, 75%, and 100% for LFP and 0%, 30%, 60%, 80%, and 100% for LCO. Each SOC condition was tested between three and six times, with some tests discarded due to instrument malfunction.

2.3. Chemical Analysis

The three filters from each test were analyzed by various instruments to determine the composition of the deposited PM_{2.5}. The cellulose back filters in Channel 1 were for collecting acidic gases, and the data will be reported in a future publication. The Channel 1 Teflon filters were analyzed for deposited mass and elements, while the Channel 2 Quartz filters were analyzed for elements and carbon compounds. The Teflon filters were first equilibrated in a clean room at a controlled temperature (21.5 ± 1.5 °C) and relative humidity ($35 \pm 5\%$) before gravimetric analysis [47]. Filters were weighed before and after sampling using an XP6 microbalance (Mettler Toledo Inc., Columbus, OH, USA) with a sensitivity of ± 1 µg. This allowed for the calculation of the PM_{2.5} mass collected on the filter as well as the average mass concentration of the smoke emissions using the filter sampling volume. After being weighed, the Teflon filters were analyzed for 51 elements (sodium to uranium) by an X-ray fluorescence (XRF) analyzer (Model Epsilon 5, PANalytical, Eindhoven, The Netherlands) [48].

Half of the Channel 2 quartz filters were extracted in distilled and deionized water, and analyzed by ion chromatography (IC; Dionex ICS-6000; Thermo Fisher Scientific, San Jose, CA, USA) [49] for 11 water-soluble ions, including: lithium (Li⁺), ammonium (NH₄⁺), sodium (Na⁺), magnesium (Mg²⁺), potassium (K⁺), calcium (Ca²⁺), fluoride (F⁻), chloride (Cl⁻), nitrate (NO₃⁻), sulfate (SO₄²⁻), and phosphate (PO₄³⁻). A 0.5 cm² punch was taken from the remaining quartz filter halves and analyzed for OC, EC, and eight thermal fractions (OC1–OC4, pyrolyzed carbon [OP], and EC1–EC3) following the IMPROVE_A thermal/optical protocol using the DRI Model 2015 Multiwavelength Carbon Analyzer (Magee Scientific, Berkeley, CA, USA) [50–52]. The remaining quartz filter material was digested in a solution of 2% nitric acid (HNO₃) and 5% hydrochloric acid (HCl) and analyzed by inductively coupled plasma mass spectrometry (ICP-MS; NexIon 2000B; Perkin-Elmer, Waltham, MA, USA) for 44 elements, including ones that could not be quantified by XRF (i.e., Li, Be, Na, Mg, Pr, Nd, Pt, Bi, and Th). ICP-MS complements XRF as it has lower detection limits for rare-earth elements [48].

2.4. Data Analysis and Quality Assurance

All raw PM_{2.5} chemical composition data were first converted to filter mass loadings in µg/filter and stack mass concentrations in µg/m³. Concentration uncertainties were calculated from the propagation of analytical and sample flow volume uncertainties [53].

Mass closure was conducted to determine the proportion of the collected filter deposits accounted for by chemical analyses, which is an indicator of the data quality [54,55]. The sum of the measured chemical species was first compared to the gravimetric mass. As shown in Figure 2a,b, these two masses were highly correlated with coefficients of determination (R^2) of 0.99. The linear regression slopes were near but lower than 1, being 0.84 and 0.86 for the LFP and LCO tests, respectively, indicating that most chemical species have been measured.

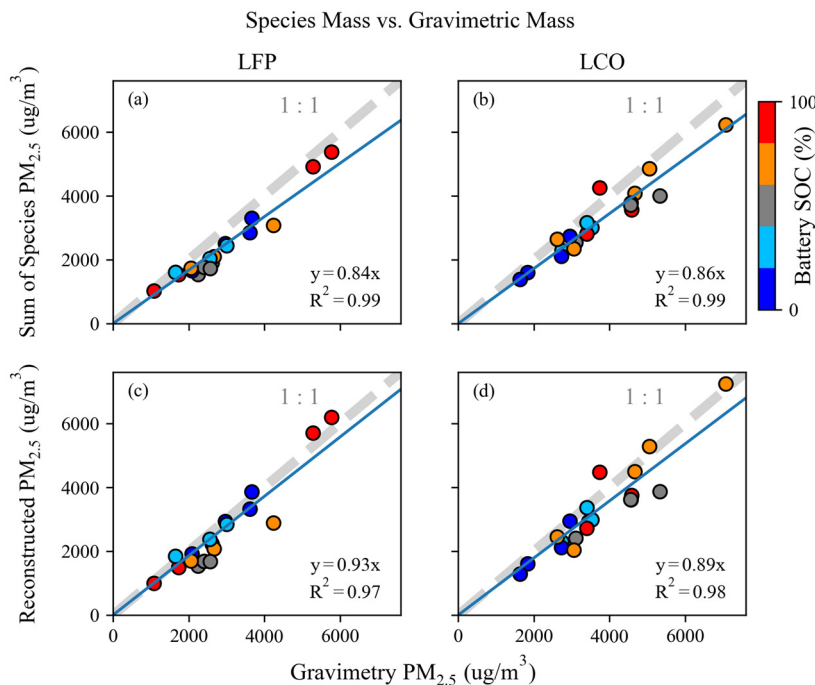


Figure 2. Comparison of chemical analysis sum of species (**a,b**) and reconstructed mass (**c,d**) with gravimetric mass for LFP (**a,c**) and LCO (**b,d**) tests.

Next, the “reconstructed” mass was compared to the measured gravimetric mass. The measured PM_{2.5} species were grouped into six major compositions: (a) organic matter (OM = OC × multiplier), (b) EC, (c) elemental phosphorus (P) that is not in PO₄³⁻ (termed P*, calculated as P from ICP-MS minus PO₄³⁻ / 3.07 from IC), (d) PO₄³⁻, (e) F⁻, and (f) other ions and elements without double counting elements present in multiple species (using the same method as for P*). The multiplier for calculating OM from OC was taken as 1.2 for fresh combustion emissions [56]. The sum of these six composition groups is defined as the reconstructed mass. The difference between the gravimetric and reconstructed masses is reported as the “unidentified” mass. Mass reconstruction attempts to account for common elements not being measured in chemical analysis, such as oxygen (e.g., in mineral oxides) and hydrogen. The slopes for reconstructed vs. gravimetric mass were 0.93 for LFP tests (Figure 2c) and 0.89 for LCO tests (Figure 2d). These relationships have similarly high R² values as the sum of species. The regression slopes being slightly below 1.0 indicates that the reconstruction assumptions mentioned above were not completely accurate for all samples. Figure S3 shows that the unidentified mass was correlated with OM (inversely) and PO₄³⁻ (directly), indicating that these species may have been the main sources of uncertainty. The reconstructed-to-gravimetric mass ratio for all tests was, however, within the acceptable range of 0.60 to 1.32 set by the U.S. EPA [57]. Mass fractions (chemical profiles) were calculated by dividing the mass of each species by the total PM_{2.5} gravimetric mass.

The balance between anions and cations was examined via ion microequivalent mole concentrations (μeq/m³), which were calculated by dividing the ion mass concentration (in μg/m³) by the ratio of atomic or molecular weight of the chemical species and the species’ charge, as shown in Equations (1) and (2) [54,56]:

$$\mu\text{eq}/\text{m}^3 \text{ for anions} = \frac{[F^-]}{19} + \frac{[Cl^-]}{35.5} + \frac{[NO_3^-]}{62} + \frac{[SO_4^{2-}]}{96/2} + \frac{[PO_4^{3-}]}{95/3} \quad (1)$$

$$\mu\text{eq}/\text{m}^3 \text{ for cations} = \frac{[Li^+]}{6.9} + \frac{[NH_4^+]}{18} + \frac{[Na^+]}{23} + \frac{[Mg^{2+}]}{24.3/2} + \frac{[K^+]}{39.1} + \frac{[Ca^{2+}]}{40.1/2} \quad (2)$$

3. Results

3.1. LIB Combustion Behavior

LIB combustion behavior ranged from only venting (with no visible flames throughout the test) to mostly flaming. Most cells vented for a period immediately after the start of TR and then autoignited for the remainder of combustion. Visual examples of the two combustion phases for an LCO test are shown in Figure 3.

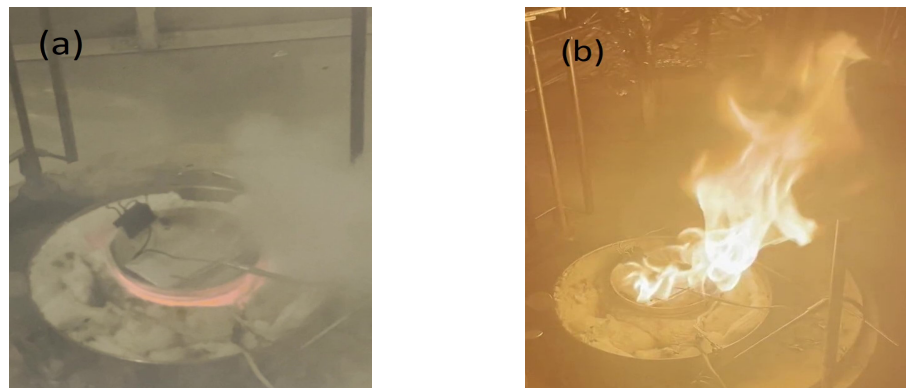


Figure 3. An example of combustion phases from an LCO test: (a) the LIB vented vigorously; and (b) the LIB burst into large flames.

Both webcam footage (Figure 3) and PM_{2.5} concentration time series measured by the ELPI+ were used to characterize the combustion behavior of each cell and estimate the proportion of PM_{2.5} emissions from venting and flaming phases, as shown in Figure 4. A threshold of 10% of the maximum PM_{2.5} concentration was used to signal the start of TR. The webcam recording was then used to determine if and when flaming started. Flaming combustion often began vigorously (as seen in Figure 3b) but quickly diminished in intensity, ending as a small, candle-sized flame that persisted well into the overall decay of PM_{2.5} concentrations. Figure 4 shows the venting and flaming phase peaks. Emissions from each phase were integrated, and the proportions of each phase to total emissions were calculated. This metric is a qualitative measure of emission proportion to characterize cell combustion characteristics and explain variations in emission profiles.

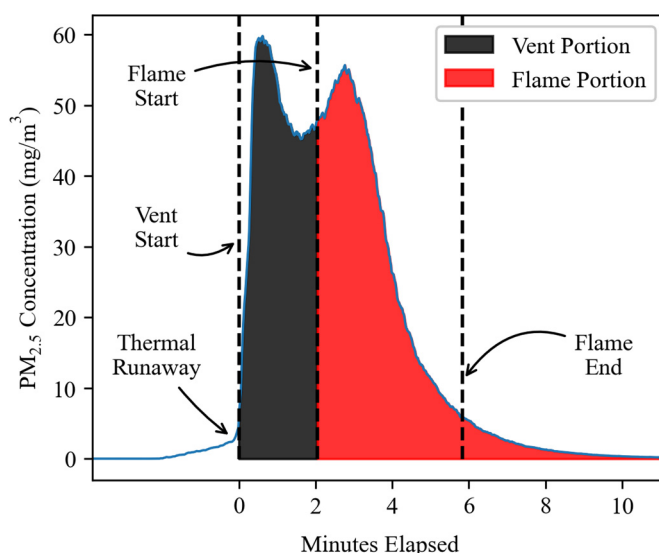


Figure 4. An example of emission allocation for the same LCO test in Figure 3, showing 44% and 56% of PM_{2.5} emissions were from venting and flaming phases, respectively. Particle concentrations are measured by ELPI+ and adjusted for sample dilution.

Figure 5a shows that LFP tests did not flame at 0% and 30% SOCs, while LCO tests flamed at all SOCs (Figure 5b). This is consistent with LFP cells having higher thermal stability compared to LCO cells. LCO tests had an increasing proportion of emissions from flaming as SOC increased, while LFP tests had the highest proportion of flaming emission at middle (50–75%) SOCs, corresponding to higher detected flame temperatures (Figure 5c). All LCO tests except one had >50% of PM_{2.5} emissions come from flaming combustion.

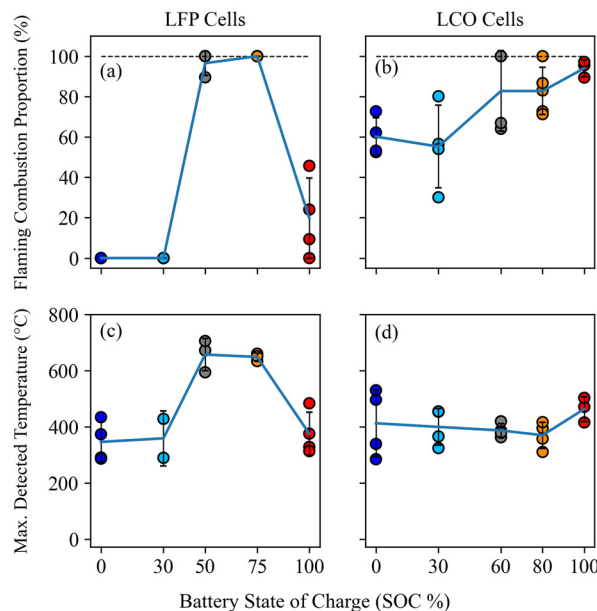


Figure 5. Proportions of PM_{2.5} emitted by flaming combustion (a,b) and maximum detected flame temperatures (c,d) for different SOCs and cell types. Symbol color represents cell SOC for each test.

3.2. Chemical Characteristics

3.2.1. Major Compositions

The six major composition groups as a percentage of gravimetric PM_{2.5} mass are shown in Figure 6 for each cell type and SOC. OM, EC, and PO₄^{3−} were the three most abundant compositions. Overall, particles from LFP tests had higher OM and lower EC compared to LCO tests. P* was mostly present in LCO tests.

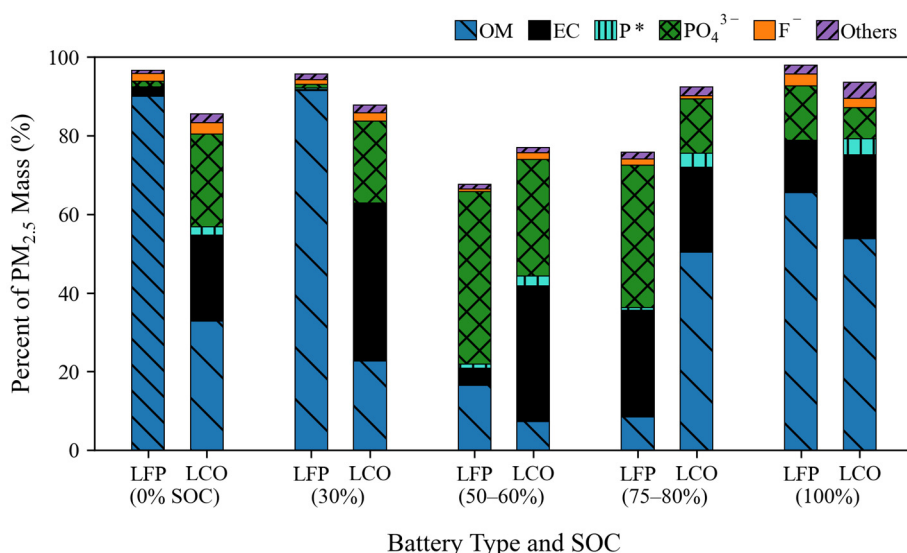


Figure 6. Average PM_{2.5} compositions as a percent of PM_{2.5} mass for LFP and LCO tests. The number of tests varied from three to five for each SOC group. P* is calculated as the difference between the total P and the P in PO₄^{3−}.

The PM_{2.5} chemical compositions of individual tests are presented in Figure 7, grouped by SOCs and cell type. Figure 7a shows that PM_{2.5} composition variation for LFP tests was low within each SOC, except among 100% SOC tests. PM_{2.5} was characterized by high OM for 0% and 30% SOC levels. EC, most dominantly produced from flaming combustion, was low for these low SOC tests but increased for SOCs above 50%. PO₄^{3−} was similarly low at 0% and 30% SOC, but other ions F[−] and Cl[−], were comparable among all SOCs.

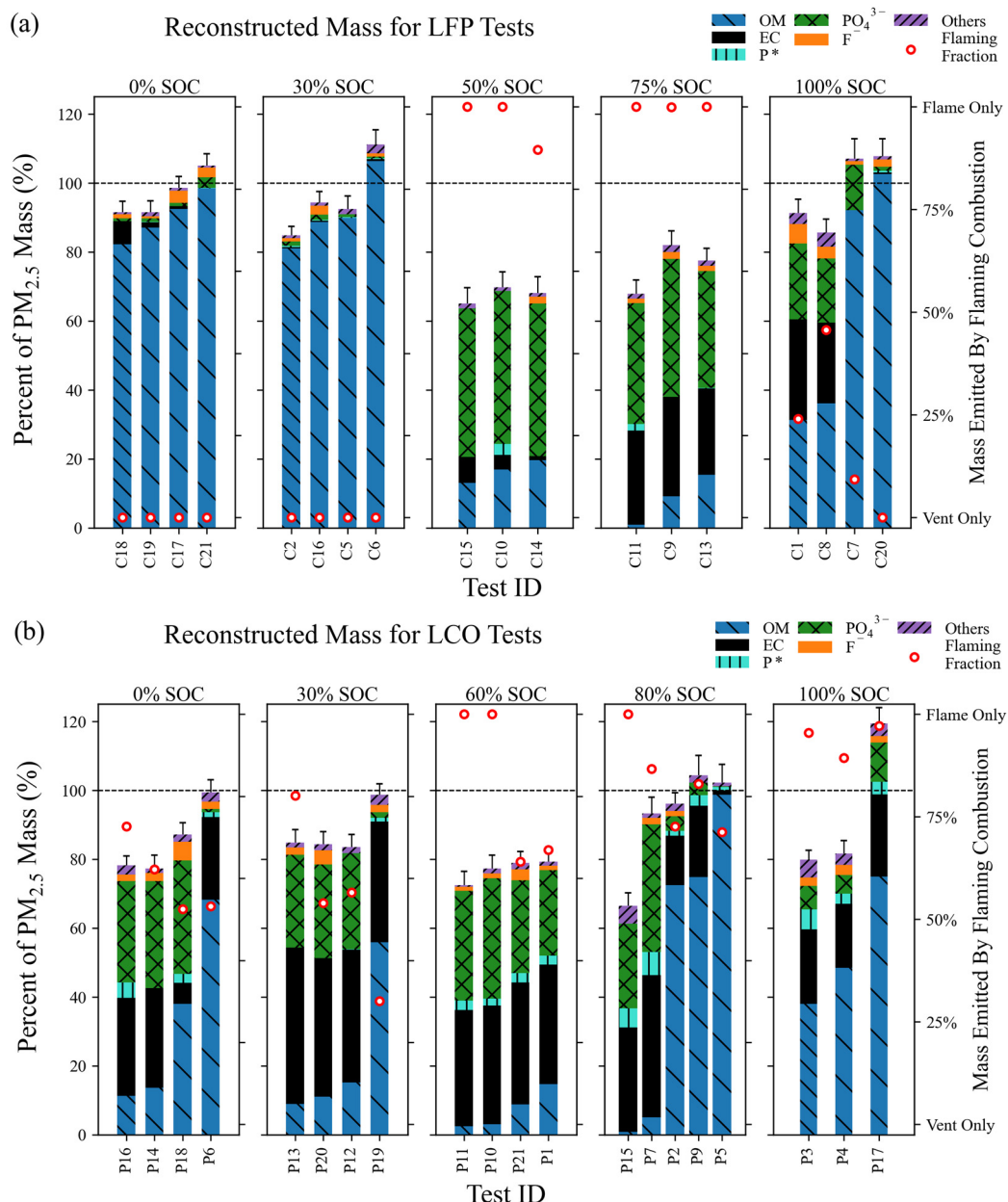


Figure 7. PM_{2.5} compositions as a percent of PM_{2.5} mass for each test of: (a) LFP and (b) LCO tests. The percentages of PM_{2.5} mass emitted in flaming phase are indicated by the red circles (right y-axis). Error bars indicate the combined uncertainty of all mass fractions in each test.

LFP tests with 50% and 75% SOCs were dominated by flaming combustion. The reconstructed mass percentages were the lowest of any test group, at ~60–80%. Compared to the 0% and 30% SOC cases, the OM fractions were much lower (1–20%), while the PO₄^{3−} fraction, practically absent in the 0% and 30% SOC cases, dominated with 34–44% of PM_{2.5} mass. The average EC fraction increased from 0–7% for 0–50% SOC to 25–29% for 75% SOC.

The shift in OM, EC, and PO_4^{3-} mass fractions was likely caused by a more energetic TR process due to increased cell energy as well as the ignition of the emissions stream.

LFP tests with 100% SOC exhibited two different combustion behaviors: Tests C1 and C8 had 24–46% emissions from flaming, while emissions from Tests C7 and C20 were dominated by venting (0–9% of emissions from flaming). The 100% SOC $\text{PM}_{2.5}$ compositions had more variability but adhered to the trend that a higher proportion of flaming combustion resulted in higher EC and PO_4^{3-} mass fractions and lower OM mass fractions. The two flaming tests (Tests C1 and C8) showed similar EC abundance to the 75% SOC tests but with higher OM, F^- , and others, and lower PO_4^{3-} . The two venting tests (Tests C7 and C20), however, resembled the vented emissions from low SOCs with no EC and little PO_4^{3-} present, although C7 (13%) had over four times the PO_4^{3-} fraction of any low SOC test. This indicates that ignition of the emissions stream, rather than cell SOC, is mostly responsible for the general composition of emitted $\text{PM}_{2.5}$ particles.

$\text{PM}_{2.5}$ mass composition for LCO tests (Figure 7b) differed from that of LFP tests, (Figure 7a), with less dependence of emissions composition on cell SOC. Two groups existed within 0–80% SOCs: one with high OM (56–99%), low PO_4^{3-} (0.2–4%), and variable EC (1–35%), resembling low SOC LFP tests; and the other with lower OM (1–15%), high PO_4^{3-} (25–37%), and consistently high EC (29–45%), resembling mid-range SOC LFP tests. As with LFP tests, the mass closure was lower for this low-OM group. Higher P^* emissions occurred for most SOCs. An exception to this grouping is the 0% SOC LCO Test P18, where high PO_4^{3-} suggests high EC should be present but high OM was seen instead, a composition similar to 50% SOC LFP tests. As with LFP tests, these groupings were related to combustion behavior, with the high EC group having more flaming combustion than the high OM group. However, compared to LFP tests, this grouping was due to smaller differences in combustion behavior, as significant flaming occurred for all LCO tests. For example, significant flaming during 80% SOC LCO Test P5 resulted in a similar emissions profile to low SOC LFP tests with no flaming. This is likely due to differences in cell casing between LCO and LFP cells. The LCO cell's thin wrapper likely results in multiple venting locations, only some of which are ignited. Since all emissions are attributed to flaming once any flames are seen, this could result in a misallocation of the emission source. The LFP cell's steel case and relief vents, on the other hand, ensure venting is concentrated into a single stream, which was either ignited or not.

LCO tests with 100% SOC are somewhere between these two groups, emitting mostly OM (38–75%) but with moderate EC (19–24%) and PO_4^{3-} (5–11%) fractions. This was in contrast to tests with high OM at SOCs below 100% (i.e., Tests P2, P5, P6, P9, and P19, with P18 being the exception), where PO_4^{3-} mass fractions dropped to $\leq 2\%$. Ignoring SOC dependence, the major combustion products from the LFP and LCO tests were broadly similar, either consisting of high OM and low EC, PO_4^{3-} , and unidentified fractions (with relatively less flaming combustion); or low OM and high EC, PO_4^{3-} , and unidentified fractions (from relatively more flaming combustion). All other ions and elements only contributed to 1.4–13% (averaging 5%) of the gravimetric mass.

3.2.2. Carbon Fractions

Emitted carbon compounds were split into seven thermal fractions depending on their volatility and thermal stability, four for OC, and three for EC [50]. As shown in Figure S4, the dominant OC fractions were OC1, OC2, and OC3, accounting for $25\% \pm 8\%$, $50\% \pm 11\%$, and $23\% \pm 12\%$ of total OC on average for both cell types. OC4 was relatively low for all tests, accounting for $1.4\% \pm 1.2\%$ of OC on average. EC2 was the dominant EC fraction, accounting for 76% of total EC on average. However, while EC1 and EC3 account for only 17% and 7% of total EC on average, they could individually account for over 50% of EC for certain tests.

The SOC dependence of OC1–4 and EC1–3 is shown in Figure 8. For LFP tests (Figure 8a–d), each EC fraction was emitted by a specific combustion behavior. EC1 was emitted during venting-dominated combustion during low SOC tests and half of 100% SOC

tests. EC2 was emitted across all SOCs but was most abundant for flaming 75% and 100% SOC tests. EC3 was emitted for 50% SOC tests but much less so for 75% SOC tests, despite both being heavily flaming. LCO tests (Figure 8e–h) showed a similar pattern for EC3 as LFP tests but differed for EC1 and EC2. EC2 and EC3 were more abundant in LCO tests than in LFP tests. EC2 had the largest increase in both mass percentage and its presence for a range of SOCs, with only three tests (i.e., P2, P5, and P18) having EC2 abundances <18%. In contrast, only five LFP tests (i.e., C1, C8, C9, C11, and C13) had EC2 abundances >18%, with the rest having abundances <5%. OC1–4 varied similarly with SOC, despite large variations in total OC. This dependence of OC1–4 (Figure 8a,e) is similar to EC1 for both cell types, an understandable result given that EC1 is measured at the closest analysis temperature to the OC fractions.

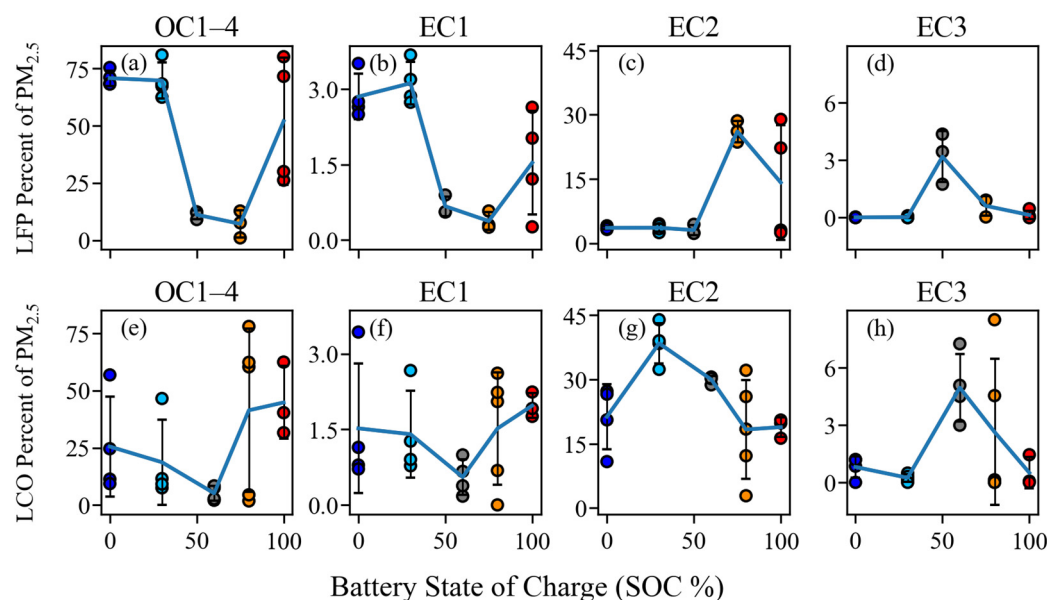


Figure 8. Dependence of total OC and EC fractions on SOC for LFP (a–d) and LCO (e–h) tests. Symbol color represents cell SOC for each test. Four OC fractions that evolved at different temperatures in a pure helium (He) carrier gas include: OC1 (140 °C), OC2 (280 °C), OC3 (480 °C), and OC4 (580 °C); three EC fractions that evolved in 98% He/2% O₂ include: EC1 (580 °C), EC2 (740 °C), and EC3 (840 °C) [50]. These fractions are indications of carbon volatility and pyrolysis and have been used to distinguish contributions to PM_{2.5} from different sources.

Carbonaceous aerosols can be generated from the combustion of graphite anodes, electrolytes, polymer separators, wrappers, and other carbon-containing components in LIBs. As electrolytes are volatile, unburnt electrolytes can contribute to OC fractions. EC2 and EC3 are refractory carbon with graphite-like structures, which may originate from the decomposition and recondensation of graphite material, as well as from high-temperature combustion [58]. Electrolyte and cathode materials may react to form carbonate, which could also contribute to various carbon fractions, depending on their decomposition temperatures. Previous studies show that polycyclic aromatic hydrocarbons (PAHs), polychlorinated biphenyls, alcohols, aldehydes, alkenes, and esters are present in particles ejected or deposited from LIB fires [20,24]. Future studies should examine the detailed composition of carbonaceous PM_{2.5} components from LIB fire emissions to assess their health effects and infer particle sources.

3.2.3. Elemental Abundances

Figures 9 and 10 show the mass fractions of 24 elements and 10 ions for the LFP and LCO tests, respectively. Elements with an average abundance of $\geq 0.001\%$ of PM_{2.5} mass for all tests were plotted. Unlike for P* and the “other” components in Figures 6 and 7, the

elemental masses within ionic compounds were not subtracted from the total measured elemental mass here. Therefore, measured elements (primarily Li, Na, Mg, P, and Ca) may have been in ionic, elemental, or oxide forms.

LFP Elements and Ions Mass Percentages

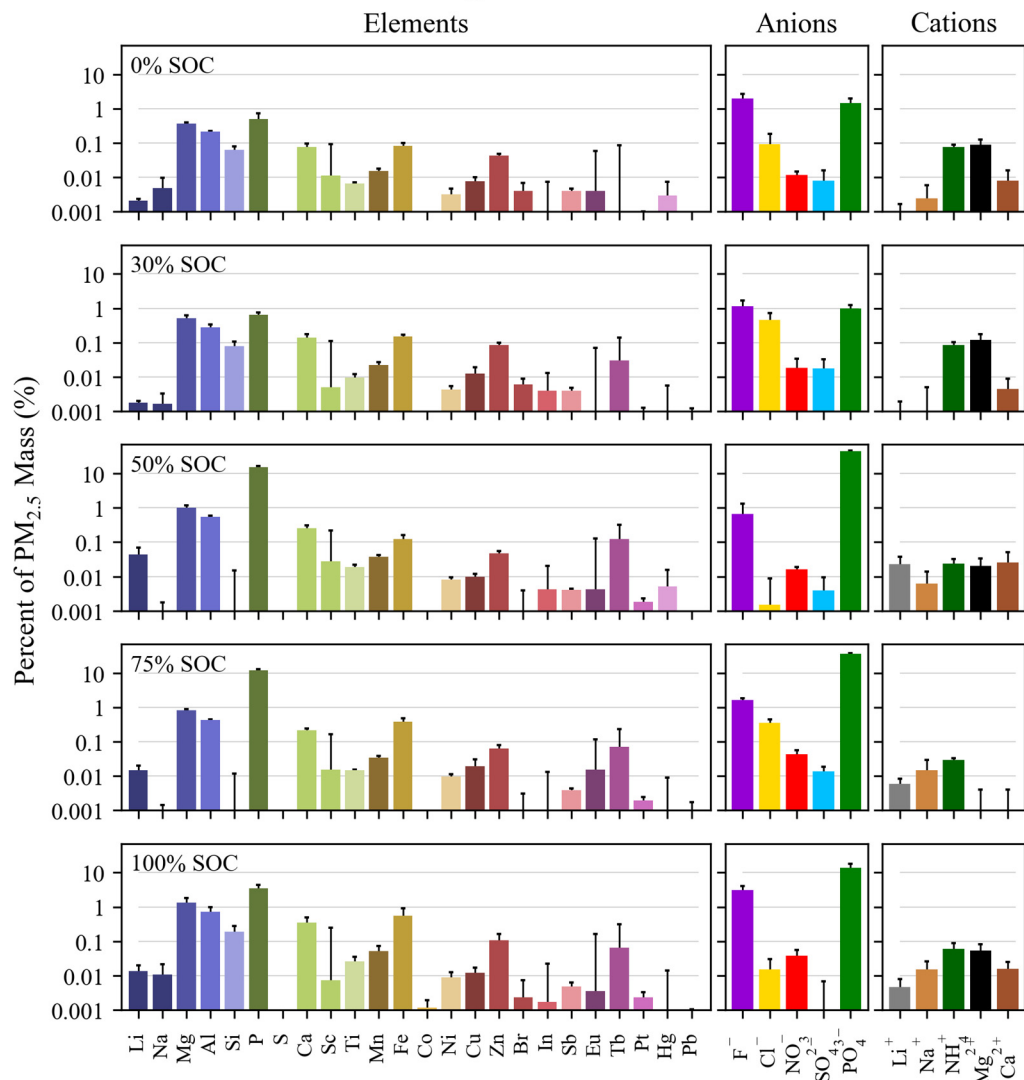


Figure 9. Average abundance (in log-scale) of elements, anions, and cations for each LFP SOC. Error bars indicate the larger of the propagated analytical uncertainty or the standard error within each SOC.

Elemental emissions for both LIB types were dominated by P, consisting of 6.4% and 8.5% of PM_{2.5} mass on average for LFP and LCO tests, respectively. PO₄³⁻ accounted for virtually all detected elemental P for LFP tests, and 77% of elemental P for LCO tests (Figure S5c,g). Other elements with significant abundance (0.1–1%) for both cell types included Mg, Al, Ca, and Fe. Li and Zn were also within this abundance range, but for LCO tests only, with Co falling just below it.

LCO Elements and Ions Mass Percentages

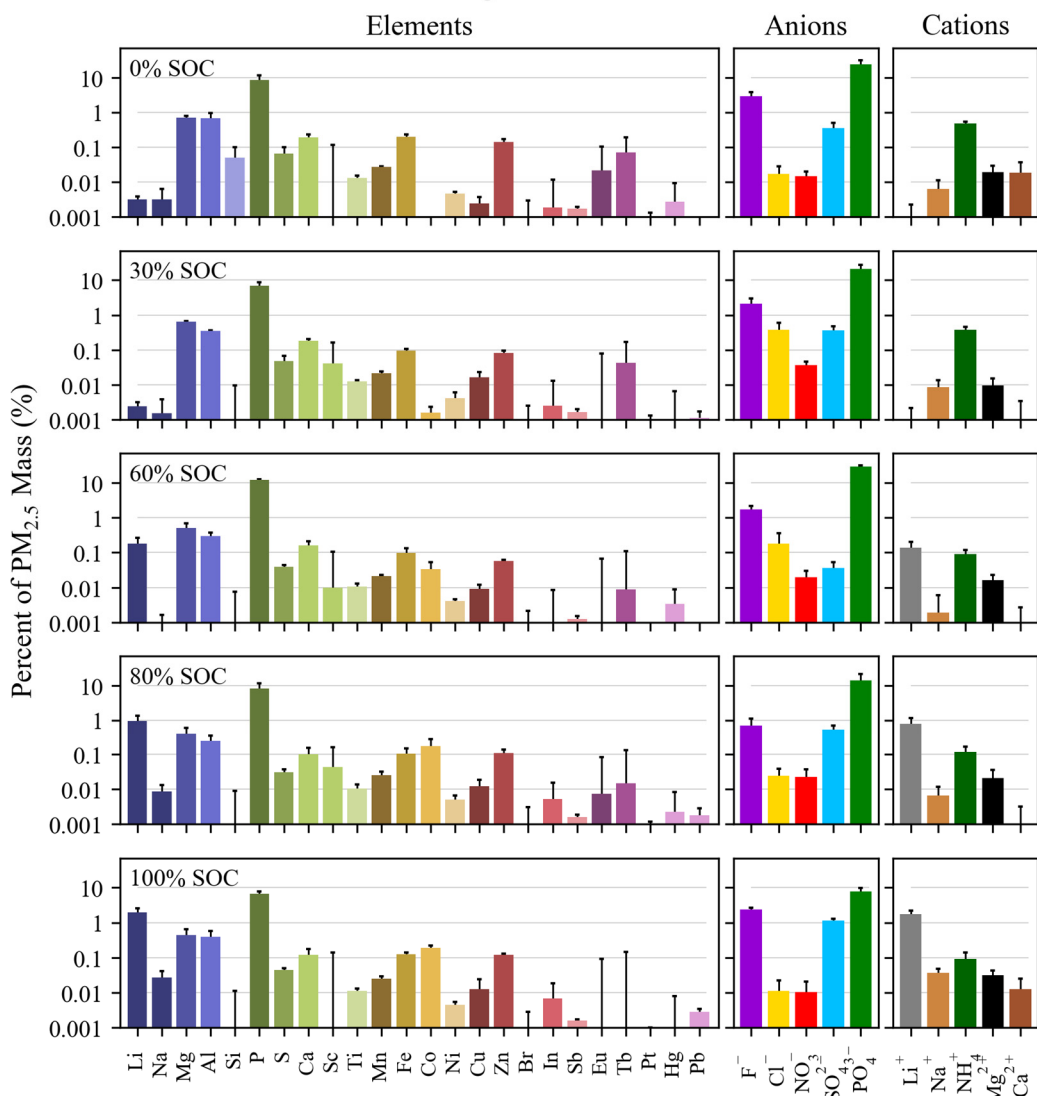


Figure 10. Average abundance (in log-scale) of elements, anions, and cations for each LCO SOC. Error bars indicate the larger of the propagated analytical uncertainty or the standard error within each SOC.

Mg was the second most abundant element after P for LFP tests (Figure 9), at 0.4–1.3%. Light metals are the next most abundant set of elements, with up to 0.7% Al, 0.6% Fe, 0.3% Ca, and 0.1% Zn. Si had maximum abundances of 0.2% but was absent from mid-SOC tests. Rare earth Tb was the only other element reaching 0.1%, while Li, Na, Sc, Ti, Mn, Ni, Cu, and Eu had maximum abundances between 0.01% and 0.1%. S, Co, Br, In, Sb, Pt, Hg, and Pb all had maximum abundances of $\leq 0.01\%$.

LCO tests (Figure 10) had higher Li abundances compared to LFP tests, reaching 2% at higher SOCs. Mg was the third most abundant element, at 0.4–0.7%. Light metal abundances were similar to LFP tests, with up to 0.7% Al, 0.2% Fe, 0.2% Ca, and 0.1% Zn. Due to its presence in the LCO cathode, Co was more abundant than for LFP tests, at up to 0.2%. The elements with maximum abundances between 0.01% and 0.1% were also similar (Na, Sc, Ti, Mn, Cu, and Eu) but included Si, S, and Tb for LCO tests. The maximum Ni abundance was half that of LFP tests (0.005%), while Br, In, Sb, Pt, Hg, and Pb were all $\leq 0.01\%$.

Table 2 compares the maximum detected abundances by SOC to literature values for total carbon (TC) and 16 elements. The measured and literature values that are most similar

are compared in the right column, giving a “best case” comparability. Measured values for Mn, Co, Ni, and Cu were much lower at 0.1–3% of the literature values. This difference may have been due to several factors. First, the relevant literature mostly involved NMC cells, so high levels of Ni, Mn, and Co are expected. Second, the larger, settleable particles that were analyzed in previous studies were likely to have metallic compositions instead of the majority of carbonaceous particles collected in this study, which were lighter and suspended in air for a longer time. This resulted in a higher average TC abundance of ~57% in this study as compared to 23–30% in most literature sources, leaving less mass to be composed of other compounds. Xu et al. [25,26], in contrast, reported much higher TC, at 90–94%, and lower metals than other sources, more similar to this study. The particles were likely in the submicron range due to a diffusion- and thermophoretic-dominated collection mechanism. The soot-dominated composition from Xu et al. could be caused by the particles being collected close to the flame before volatile compounds (e.g., phosphate) cooled down and condensed in the particle phase, which is evident from much lower P abundances than in this study. This is less representative of the composition of inhaled particulate, however, as the emission stream will most likely have cooled before inhalation.

Table 2. Comparison of maximum measured species abundance to literature values. Literature values are from NMC cell combustion with maximum collected particle sizes ranging from 200 to 15,000 μm [17,21,59,60] and LFP cell combustion with unspecified particle sizes [25,26].

Element	This Study		Literature [17,21,25,26,59,60]	Closest Factor Difference
Measure	% of PM _{2.5} Mass ($\leq 2.5 \mu\text{m}$)	% of Mass (200–15,000 μm) *	NMC and LFP	
LIB Type	LFP	LCO		
TC	58 (avg.)	56 (avg.)	23–94	0.6 \times lit. values
Li	0.044	1.98	2.9–4.0	1.3 \times lit. values
Na	0.011	0.027	0.06–0.1	0.45 \times lit. values
Mg	1.33	0.719	0.001–0.006	120 \times lit. values
Al	0.720	0.688	3.6–13.5	0.2 \times lit. values
Si	0.193	0.050	0.025	2 \times lit. values
P	15.1	12.2	0.02–2.2	5.6 \times lit. values
S	0	0.066	0.3–0.9	0.22 \times lit. values
Ca	0.354	0.191	0.04–0.05	3.8 \times lit. values
Ti	0.026	0.013	0.003–0.01	1.3 \times lit. values
Mn	0.051	0.027	5.2–13.1	0.01 \times lit. values
Fe	0.553	0.201	0.07–0.5	1.1 \times lit. values
Co	0.001	0.191	5.9–10.5	0.032 \times lit. values
Ni	0.010	0.005	18–51	0.001 \times lit. values
Cu	0.020	0.016	2.2–9.5	0.009 \times lit. values
Zn	0.108	0.141	0.001–0.008	14 \times lit. values
Br	0.006	0.001	0.01–0.04	0.61 \times lit. values

* Refs. [25,26] did not specify particle size. Since particles were collected near the flame with the dominant deposition mechanisms of diffusion and thermophoresis, the particles are expected to be in the submicron size range.

Values for Li, Na, Al, S, Ti, Fe, Br, and Sb were more similar at 20–130% of literature values. Finally, some light elements had larger abundances than literature values, with Mg, Si, P, Ca, and Zn having 120-, 2-, 6-, 4-, and 14-times higher abundances, respectively. The differences in elemental composition from different studies can be caused by several factors, including cell chemistry/age/SOC, combustion conditions, sampling methods, particle size ranges, and analytical methods.

Figures 11 and 12 show SOC dependence for abundant elements or those with interesting behavior for LFP and LCO tests, respectively. Both show the same species except that Ni is shown for LFP tests, while Co is shown for LCO tests. As shown in Figure 11, many elements have a positive correlation with SOC for LFP tests. Mg, Al, Ca, Fe, Ni, Zn, as well as Ti, Mn, Pt, and, to a lesser extent, Li, Co, and Cu, all increased with SOC. Variability was

high at 100% SOC, but the trend is still clear. SOC dependence of P was quite different, with none found at low SOCs and then the abundance peaking at 50% SOC before dropping below one-third the peak value at 100% SOC. The positive correlation of many elements is interesting, as both the maximum temperature detected and the proportion of flaming combustion (Figure 5) peaked abruptly at mid-range SOCs and then dropped for 100% SOC, matching the behavior of P. The SOC dependence of P matching that of cell temperature indicates that the thermally stable LFP cathode decomposed at the expected ~500 °C [35]. The difference in SOC dependence for the other elements indicates that internal changes other than just hotter or more flaming combustion may be occurring with increasing SOC.

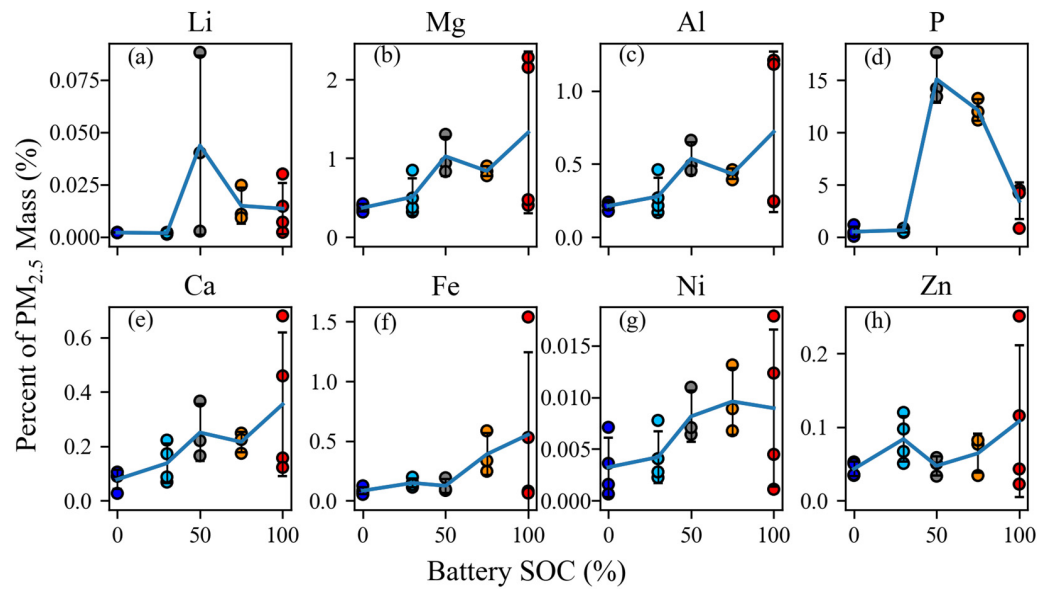


Figure 11. Dependence of element abundance on SOC for LFP tests for Li (a), Mg (b), Al (c), P (d), Ca (e), Fe (f), Ni (g), and Zn (h). Symbol color represents SOC.

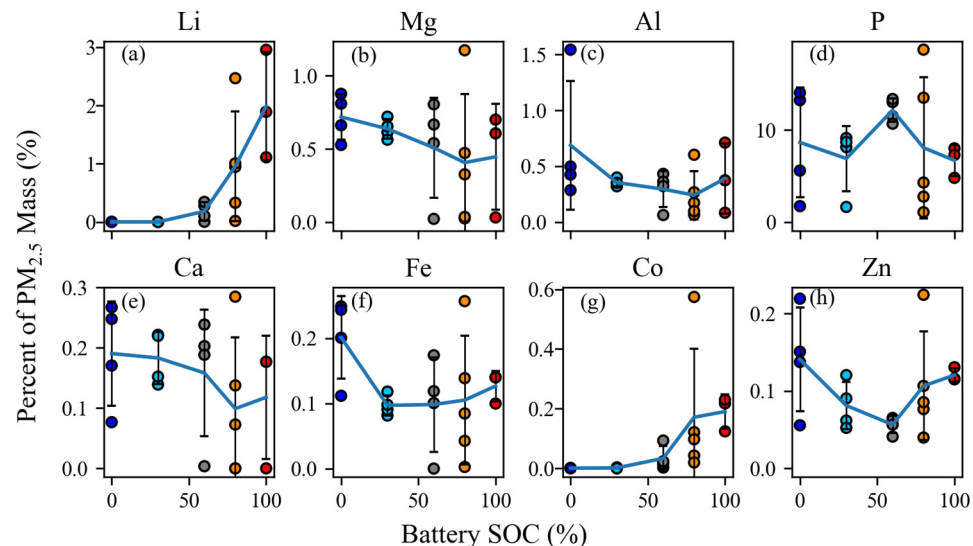


Figure 12. Dependence of element abundance on SOC for LCO tests for Li (a), Mg (b), Al (c), P (d), Ca (e), Fe (f), Co (g), and Zn (h). Symbol color represents SOC.

For LCO tests, Figure 12 shows that fewer elements (Li and Co) exhibited a positive correlation with SOC. Instead, many elements (Mg, Al, Ca, Fe, and Zn) were most abundant at 0% SOC and least abundant at 60% SOC, increasing again thereafter. P abundance is variable for LCO cell tests, with no clear dependence on SOC due to the variable combustion

behavior effects discussed in Section 3.2.1. That Li and Co increased with SOC indicates that the LIB anode and cathode underwent more decomposition at higher SOCs despite constant flame temperatures of ~ 400 °C (Figure 5), contrasting with the abrupt temperature changes for LFP tests. This may be due to the primary flame jet missing the thermocouple during LCO cell tests, resulting in an undermeasurement of peak flame temperatures. The fraction of PM_{2.5} emitted from flaming combustion, however, increased with SOC (Figure 5b).

3.2.4. Water-Soluble Ions

Water-soluble anions and cations are shown alongside element abundances in Figures 9 and 10. PO₄³⁻ was by far the dominant ion in PM_{2.5} for LFP tests (14–44% abundance) at 50% SOC and above, and LCO tests (8–30% abundance) for all SOCs. For LFP tests at low SOCs, PO₄³⁻ and F⁻ abundances were similar at 1–2%. F⁻ was the second most abundant ion at 0.7–3% for both cell types, followed by Cl⁻ for LFP tests (up to 0.5%) and Li⁺ for LCO tests (up to 1.7%). Other notable abundances were SO₄²⁻ (0.5–1.1%) for LCO tests at high SOC and Cl⁻ and ammonium (NH₄⁺) for LCO tests (up to 0.4–0.5%). All other ions had maximum abundances of $\leq 0.1\%$.

The ratios of ion abundance over that of corresponding elements were variable. Li⁺ made up only 40% of total Li for LFP tests but reached 87% for LCO tests (Figure S5, ratio does depend on SOC as seen in Figure S6). Mg was predominantly nonionic, while the P contained in PO₄³⁻ accounted for $\sim 100\%$ and 77% of the total P for LFP and LCO tests, respectively. The S in SO₄²⁻ was consistently higher than total elemental S for LCO tests, especially at high SOCs (Figure S5h). This suggests that some sulfur compounds might have evaporated in the vacuum of the XRF instrument.

Abundance dependences on SOC are shown for some ions in Figure 13a–d for LFP and Figure 13e–h for LCO tests. F⁻ variability was high, but abundance tended to be low for mid-range SOCs and higher for low, and high, SOCs. SO₄²⁻ increased significantly for >60% SOC in LCO tests but had no SOC dependence for LFP tests. PO₄³⁻ dependence on SOC resembled that of P seen in Figures 11 and 12, except that a noticeable downward correlation was seen for LCO tests. NH₄⁺ abundance was highest at low SOCs for both cell types and decreased for mid-range SOCs, especially in LCO tests, likely because NH₄⁺ decomposes at high flaming temperatures.

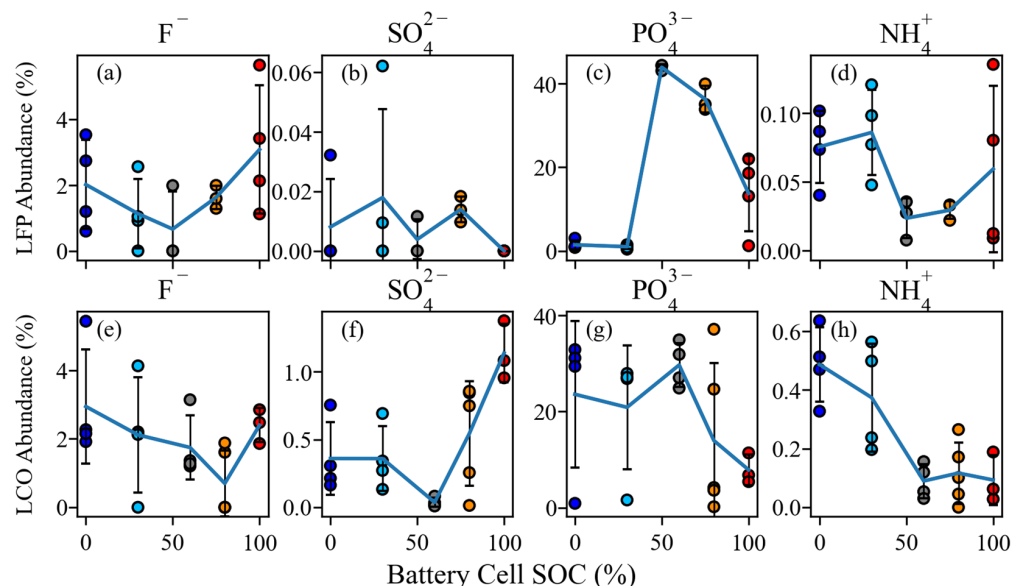


Figure 13. Dependence of ion abundance on SOC for LFP (a–d) and LCO (e–h) tests. Symbol color represents cell SOC for each test.

Figure 14 shows the anion and cation balances for each test. The ratio of anion to cation abundance indicates degrees of acidity or alkalinity since H^+ or OH^- were not directly measured [54,56]. For LFP tests, the anion/cation ratio ranges depended on combustion behavior, with ~10:1 for venting tests and ~200:1 for tests with significant flaming. It initially appears there is a correlation to SOC in Figure 14a, but the two 100% SOC outliers (labeled Tests C20 and C7, which are nonflaming tests with high OM as shown in Figure 7a) show the underlying trend was actually due to combustion behavior (Figure 14c). In contrast, LCO anion/cation ratios were directly dependent on SOC. With one exception (Test P7), 80–100% SOCs had ratios just above 1:1, while 0–60% SOCs had ratios near 20:1. Heavily flaming LCO tests had lower ratios on average, but could be present in both groups.

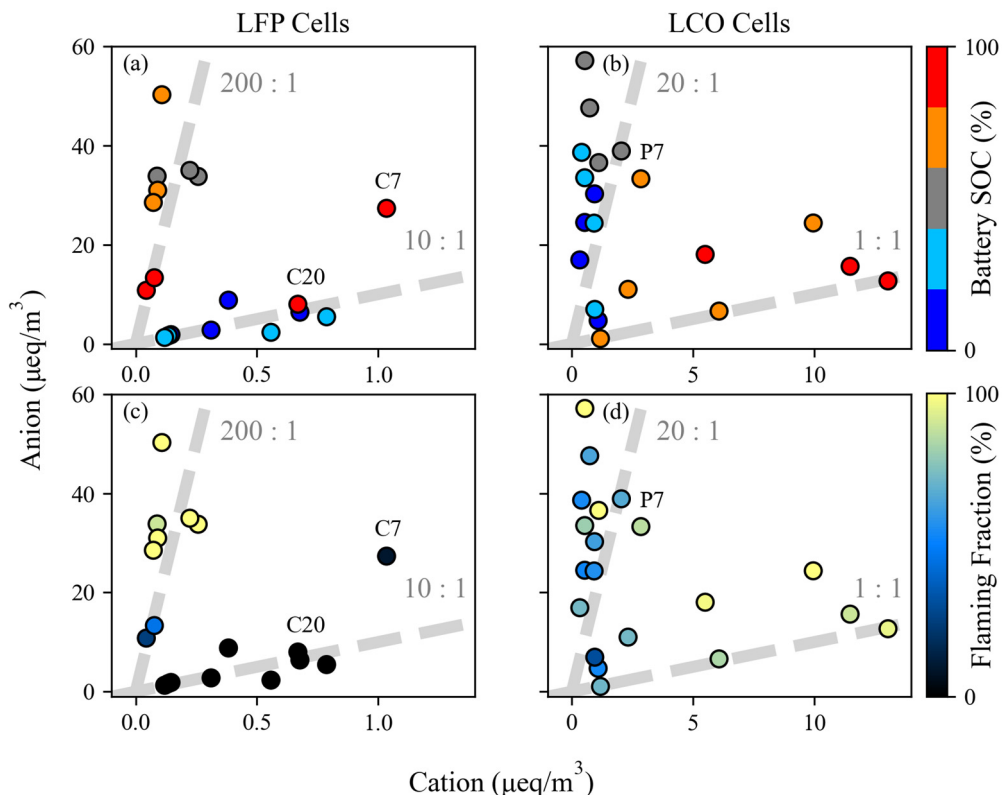


Figure 14. Anion and cation microequivalent (μeq) concentration relationships for LFP (a,c) and LCO (b,d) tests. Each test is color coded for SOC (a,b) or flaming fraction (c,d).

Anion/cation ratios > 1.0 indicate that the particles were acidic. Held et al. [20] analyzed ion concentrations in sprinkler water used to extinguish an NMC LIB fire and in storage water that the LIB was submerged in after extinguishing. They found that the sprinkling water was moderately alkaline, with a pH value of 8, while the storage water was highly alkaline, with a pH value of 12. The different acidity between the PM_{2.5} measured in this study and the water analysis by Held et al. [20] could be caused by different battery chemistry (Held et al. did not detect PO_4^{3-}) as well as the different compositions of particles and process water.

Figure 15 shows a much higher abundance of particulate anions than cations. PO_4^{3-} was excluded from the anions to allow the relative abundances of other ions to be seen. F^- dominated non- PO_4^{3-} anion abundance, while Li^+ was only present in high SOC LCO tests. Mg^{2+} and NH_4^+ were the dominant cations except for high SOC LCO tests, which have elevated Li^+ . A greater SO_4^{2-} abundance for LCO than LFP tests can also be seen.

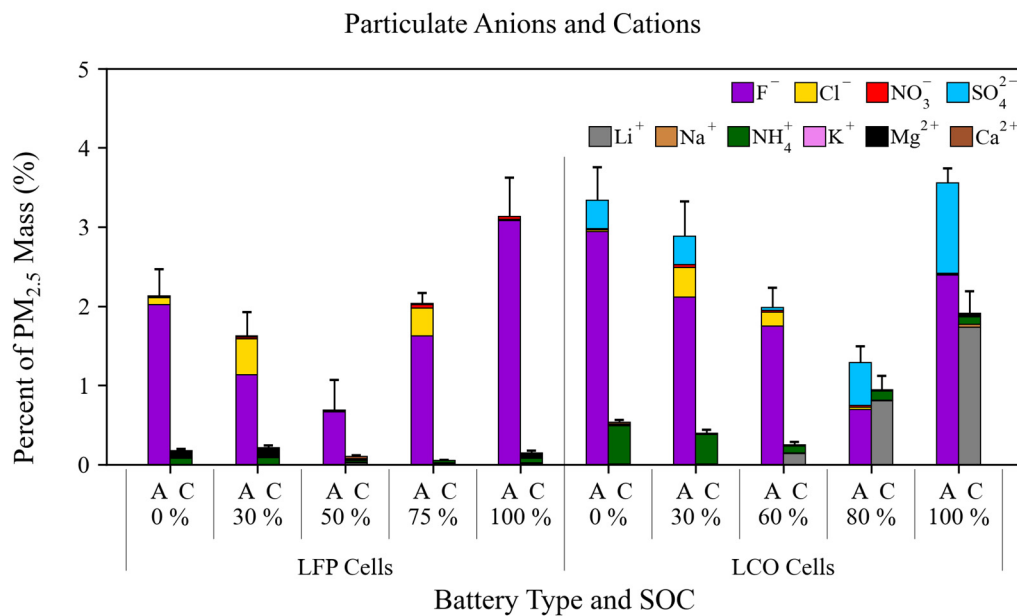


Figure 15. Abundance comparisons of particulate anions and cations (“A” and “C”) for each cell type and SOC. The error bars represent the larger of the propagated analytical uncertainty or the standard error within each SOC.

3.2.5. Comparison with Previous Studies

The mass fractions of major emission components are compared to the literature values in Table 3. Average values for LFP tests at 100% SOC were used to most closely match tests in the literature. Only one study [19] reported carbon fractions (also for LFP cells), while others [17,20,21,24,59] reported the mass fraction of EC (all for NMC cells). PO₄³⁻ and F⁻ were reported by Held et al. [20], while elemental P and F were reported by others [17,21,26,59–61]. The collected particle sizes were much larger than PM_{2.5} in most literature, resulting in much higher metal mass fractions due to enriched compositions from electrodes, current collectors, and casings [23]. The smaller particles are expected to contain more combustion products, including organic compounds, EC, and PO₄³⁻.

Table 3. Mass fraction comparison to literature values.

Reference	SOC and Cell Type	Max Particle Size (μm)	Total Carbon	EC/OC	Total P	F and F ⁻	Other Metals
This study	100% LFP	2.5	68	16/52	3.4	3.1 (F ⁻)	2
[17]	100% NMC	850	30		0.55	0.002	42
[19]	100% LFP	2.5	63	20/43			
[20]	100% NMC	Settleable	10–15			2.5 (F ⁻)	24
[21]	100% NMC	850	23		0.81	0.60	63
[24]	Var. NMC	Settleable	68				27
[25,26]	100% LFP	Soot	90–94		0.02–0.1	1–2	<2
[59]	100% NMC	Settleable	28		0.31	0.34	57
[60]	100% NMC	200			2.2	4.1	92
[62]	100% NMC	50					53

OC and EC carbon fractions from this study compared well to those from Premnath et al. [19], who also measured PM_{2.5} particles. Held et al. [20] found that the carbon content of soot increased from 1–5% at a distance of 1 m to 10–15% at 50 m from the battery fire, indicating that smaller particles, which remain suspended longer after being emitted, contained more carbon. The nucleation and condensation of carbonaceous materials upon cooling will also generate smaller particles further away from the fire. Xu et al. [25,26] found very high carbon content (90–94%) for soot particles collected near the flame, likely

dominated by EC. F and total metal contents are more similar to our findings than other studies. Total P and F^- from this study compared well with literature values, but no published airborne PO_4^{3-} mass fractions were found.

4. Discussion and Conclusions

LIB fires emit a large number of particles over a wide size range. While several past studies have examined the chemical properties of larger particles, few studies have examined the properties of $\text{PM}_{2.5}$. These fine particles are of special concern because they can be inhaled into the human respiratory track and cause adverse health effects [26]. The chemical compositions of $\text{PM}_{2.5}$ are also important for improving fire detection, designing proper personal protection equipment for people near fires, such as emergency responders, and implementing proper postfire cleanup. This study fills the chemical composition knowledge gap for $\text{PM}_{2.5}$ emitted from the combustion of two types of LIBs at various SOCs.

Key characteristics of LIB combustion behaviors and the composition of emitted $\text{PM}_{2.5}$ are:

- (1) Consistent with the higher thermal stability of LFP than LCO cells, LFP tests did not flame at 0% and 30% SOCs, while LCO tests flamed at all SOCs. LCO tests had more emissions from flaming as SOC increased, while LFP tests had the highest proportion of flaming emissions at 50% and 75% SOCs when higher flame temperatures were detected.
- (2) The chemical composition of the $\text{PM}_{2.5}$ emitted from LIB combustion was dominated by OM, EC, and PO_4^{3-} . While OM was mostly emitted through cell venting, EC and PO_4^{3-} were generated from flaming combustion. Particles from LFP tests had higher OM but lower EC than those from LCO tests.
- (3) OC1–3 fractions that volatilize at a range of temperatures (140–480 °C) were abundant, indicating the presence of a variety of organic compounds. The high abundance of EC2 and the presence of EC3 in some tests are indicators of high combustion temperatures.
- (4) Metals were present in small proportions of $\text{PM}_{2.5}$ mass, with the most abundant being Li, Mg, Al, Ca, Fe, and Zn. LCO tests had higher Li and Co abundances than LFP tests, and both elements exhibited a positive correlation with SOC. LFP had more elements (e.g., Mg, Al, Ca, Fe, Ni, and Zn) that increased in abundance with SOC. The metal abundances in $\text{PM}_{2.5}$ were much lower than those reported for larger, settleable particles.
- (5) Ionic compounds other than PO_4^{3-} were detected, primarily F^- with lower abundances of Cl^- and SO_4^{2-} . The balance between water-soluble anion and cation species indicates that the freshly emitted particles were strongly acidic.
- (6) While multiple tests within the same nominal conditions (LIB cell type and SOC) showed mostly consistent $\text{PM}_{2.5}$ characteristics, some variations were observed. In addition to cell chemistry and SOC, the $\text{PM}_{2.5}$ composition was also affected by the combustion behavior, such as the fraction of vented emission streams that were ignited and combustion temperatures.

The detailed $\text{PM}_{2.5}$ chemical compositions and their variation with cell chemistry, SOC, and combustion behavior will allow emergency responders, LIB manufacturers, and responsible authorities to plan for and respond to LIB fires. The toxicity of the emitted organics, ionic compounds, and phosphorus and lithium compounds warrants further research. Future research should also address the interaction between fire suppression methods and LIB fires, for example, water mist might temporarily intensify fires and increase hydrogen fluoride emissions [63,64]. Finally, using data from this study to investigate cell chemistry, electrochemical reactions, and combustion processes may lead to improved LIB designs.

Supplementary Materials: The following supporting information can be downloaded at: <https://www.mdpi.com/article/10.3390/batteries10090301/s1>, Supplementary Captions. Figure S1: The two LIB types tested; Figure S2: A comparison of LFP and LCO cell characteristics and performance metrics; Figure S3: Correlation between unidentified portion of reconstructed mass and selected mass

fractions; Figure S4: Thermal carbon fractions as a percent of PM_{2.5} mass; Figure S5: Proportions of total elemental abundance attributed to ionic compounds; and Figure S6: Dependence of ion/element ratios on cell SOC [50,65,66].

Author Contributions: Conceptualization, X.W.; Methodology, M.C. and X.W.; Software, M.C.; Validation, M.C. and X.W.; Formal Analysis, M.C.; Investigation, M.C., B.B. and X.W.; Resources, X.W.; Data Curation, M.C.; Writing—Original Draft Preparation, M.C. and X.W.; Writing—Review and Editing, X.W., J.C.C., J.G.W. and Y.W.; Visualization, M.C.; Supervision, X.W. and Y.W.; Project Administration, X.W.; Funding Acquisition, X.W. All authors have read and agreed to the published version of the manuscript.

Funding: This research was funded by the U.S. National Aeronautics and Space Administration's Established Program to Stimulate Competitive Research, CAN Grant No. 80NSSC19M0152 and Nevada Space Grant No. 80NSSC20M0043 22–24.

Data Availability Statement: The raw data supporting the conclusions of this article will be made available by the authors on request. Calculated emission factors for all measured species are included in the Supplementary Material.

Acknowledgments: The authors thank Hans Moosmüller for the use of the burn chamber where experiments were performed and DRI personnel for support and filter analysis.

Conflicts of Interest: The authors declare no conflicts of interest.

Abbreviations

μeq	microequivalent
Al	aluminum
Br	bromine
Ca	calcium
Ca ²⁺	calcium ion
Cl ⁻	chloride
Co	cobalt
Cu	copper
DRI	Desert Research Institute
EC	elemental carbon
EC1	elemental carbon evolved at 580 °C
EC2	elemental carbon evolved at 740 °C
EC3	elemental carbon evolved at 840 °C
EDX	energy dispersive X-ray analysis
ELPI	electrical low-pressure impactor
EPA	Environmental Protection Agency
Eu	europium
EV	electric vehicle
F ⁻	fluoride
FAA	Federal Aviation Administration
Fe	iron
HCl	hydrochloric acid
Hg	mercury
HNO ₃	nitric acid
IC	ion chromatography
ICP-MS	inductively coupled plasma mass spectrometry
In	indium
K ⁺	potassium ion
LCO	lithium cobalt oxide
Li	lithium

Li^+	lithium ion
LIB	lithium-ion battery
LFP	lithium iron phosphate
Mg	magnesium
Mg^{2+}	magnesium ion
Mn	manganese
MW	megawatt
Na	sodium
Na^+	sodium ion
NASA	National Aeronautics and Space Administration
NH_4^+	ammonium
Ni	nickel
NMC	nickel manganese cobalt oxide
NO_3^-	nitrate
OC	organic carbon
OC1	organic carbon evolved at 140 °C
OC2	organic carbon evolved at 280 °C
OC3	organic carbon evolved at 480 °C
OC4	organic carbon evolved at 580 °C
OP	pyrolyzed carbon
OM	organic matter
P	phosphorus
PAH	polycyclic aromatic hydrocarbons
Pb	lead
PM	particulate matter
PM_x	particles with aerodynamic diameters $\leq x \mu\text{m}$
PO_4^{3-}	phosphate
Pt	platinum
S	sulfur
Sb	antimony
Sc	scandium
Si	silicon
SO_4^{2-}	sulfate
SOC	state of charge
SEM	scanning electron microscopy
TC	total carbon
Tb	terbium
Ti	titanium
TR	thermal runaway
XRF	X-ray fluorescence
Zn	zinc

References

1. Doughty, D.H.; Roth, E.P. A General Discussion of Li Ion Battery Safety. *Electrochim. Soc. Interface* **2012**, *21*, 37–44. [[CrossRef](#)]
2. Feng, X.; Ouyang, M.; Liu, X.; Lu, L.; Xia, Y.; He, X. Thermal runaway mechanism of lithium ion battery for electric vehicles: A review. *Energy Storage Mater.* **2018**, *10*, 246–267. [[CrossRef](#)]
3. EVFireSafe. Source: evfiresafe.com. Available online: <https://www.evfiresafe.com/> (accessed on 31 October 2023).
4. FAA. Events with Smoke, Fire, Extreme Heat or Explosion Involving Lithium Batteries Federal Aviation Administration. Available online: https://www.faa.gov/hazmat/resources/lithium_batteries/media/Battery_incident_chart.pdf (accessed on 8 February 2020).
5. NASA. Lithium-Ion Battery Fire; 3516; National Aeronautics and Space Administration: Public Lessons Learned System. Available online: <https://llis.nasa.gov/lesson/3516> (accessed on 1 February 2024).
6. Nigl, T.; Baldauf, M.; Hohenberger, M.; Pomberger, R. Lithium-Ion Batteries as Ignition Sources in Waste Treatment Processes—A Semi-Quantitative Risk Analysis and Assessment of Battery-Caused Waste Fires. *Processes* **2020**, *9*, 49. [[CrossRef](#)]
7. U.S. EPA. *An Analysis of Lithium-Ion Battery Fires in Waste Management and Recycling; Office of Resource Conservation and Recovery*; U.S. Environmental Protection Agency: Washington, DC, USA, 2021. Available online: https://www.epa.gov/system/files/documents/2021-08/lithium-ion-battery-report-update-7.01_508.pdf (accessed on 1 February 2024).

8. Yuan, L.; Dubaniewicz, T.; Zlochower, I.; Thomas, R.; Rayyan, N. Experimental study on thermal runaway and vented gases of lithium-ion cells. *Process Saf. Environ. Prot.* **2020**, *144*, 186–192. [[CrossRef](#)]
9. Nedjalkov, A.; Meyer, J.; Köhring, M.; Doering, A.; Angelmahr, M.; Dahle, S.; Sander, A.; Fischer, A.; Schade, W. Toxic gas emissions from damaged lithium ion batteries—Analysis and safety enhancement solution. *Batteries* **2016**, *2*, 5. [[CrossRef](#)]
10. Larsson, F.; Andersson, P.; Blomqvist, P.; Mellander, B.-E. Toxic fluoride gas emissions from lithium-ion battery fires. *Sci. Rep.* **2017**, *7*, 10018. [[CrossRef](#)]
11. Essl, C.; Seifert, L.; Rabe, M.; Fuchs, A. Early Detection of Failing Automotive Batteries Using Gas Sensors. *Batteries* **2021**, *7*, 25. [[CrossRef](#)]
12. Koch, S.; Fill, A.; Birke, K.P. Comprehensive gas analysis on large scale automotive lithium-ion cells in thermal runaway. *J. Power Sources* **2018**, *398*, 106–112. [[CrossRef](#)]
13. Fernandes, Y.; Bry, A.; De Persis, S. Identification and quantification of gases emitted during abuse tests by overcharge of a commercial Li-ion battery. *J. Power Sources* **2018**, *389*, 106–119. [[CrossRef](#)]
14. Willstrand, O.; Pushp, M.; Andersson, P.; Brandell, D. Impact of different Li-ion cell test conditions on thermal runaway characteristics and gas release measurements. *J. Energy Storage* **2023**, *68*, 107785. [[CrossRef](#)]
15. Baird, A.R.; Archibald, E.J.; Marr, K.C.; Ezekoye, O.A. Explosion hazards from lithium-ion battery vent gas. *J. Power Sources* **2020**, *446*, 227257. [[CrossRef](#)]
16. Sun, J.; Li, J.; Zhou, T.; Yang, K.; Wei, S.; Tang, N.; Dang, N.; Li, H.; Qiu, X.; Chen, L. Toxicity, a serious concern of thermal runaway from commercial Li-ion battery. *Nano Energy* **2016**, *27*, 313–319. [[CrossRef](#)]
17. Zhang, Y.; Wang, H.; Li, W.; Li, C.; Ouyang, M. Size distribution and elemental composition of vent particles from abused prismatic Ni-rich automotive lithium-ion batteries. *J. Energy Storage* **2019**, *26*, 100991. [[CrossRef](#)]
18. Barone, T.L.; Dubaniewicz, T.H.; Friend, S.A.; Zlochower, I.A.; Bugarski, A.D.; Rayyan, N.S. Lithium-ion battery explosion aerosols: Morphology and elemental composition. *Aerosol Sci. Technol.* **2021**, *55*, 1183–1201. [[CrossRef](#)] [[PubMed](#)]
19. Premnath, V.; Wang, Y.; Wright, N.; Khalek, I.; Uribe, S. Detailed characterization of particle emissions from battery fires. *Aerosol Sci. Technol.* **2022**, *56*, 337–354. [[CrossRef](#)]
20. Held, M.; Tuchschmid, M.; Zennegg, M.; Figi, R.; Schreiner, C.; Mellert, L.D.; Welte, U.; Kompatscher, M.; Hermann, M.; Nacheff, L. Thermal runaway and fire of electric vehicle lithium-ion battery and contamination of infrastructure facility. *Renew. Sustain. Energy Rev.* **2022**, *165*, 112474. [[CrossRef](#)]
21. Wang, H.; Wang, Q.; Jin, C.; Xu, C.; Zhao, Y.; Li, Y.; Zhong, C.; Feng, X. Detailed characterization of particle emissions due to thermal failure of batteries with different cathodes. *J. Hazard. Mater.* **2023**, *458*, 131646. [[CrossRef](#)]
22. Padilla, R.E.; Meyer, M.; Dietrich, D.L.; Ruff, G.A.; Urban, D.L. Hazardous Effects of Li-Ion Battery Based Fires. In Proceedings of the 50th International Conference on Environmental Systems, Boston, MA, USA, 12–16 July 2020.
23. Li, W.; Xue, Y.; Feng, X.; Rao, S.; Zhang, T.; Gao, Z.; Guo, Y.; Zhou, H.; Zhao, H.; Song, Z.; et al. Characteristics of particle emissions from lithium-ion batteries during thermal runaway: A review. *J. Energy Storage* **2024**, *78*, 109980. [[CrossRef](#)]
24. Chen, S.; Wang, Z.; Yan, W. Identification and characteristic analysis of powder ejected from a lithium ion battery during thermal runaway at elevated temperatures. *J. Hazard. Mater.* **2020**, *400*, 123169. [[CrossRef](#)]
25. Xu, Y.; Wang, Y.; Chen, X.; Pang, K.; Deng, B.; Han, Z.; Shao, J.; Qian, K.; Chen, D. Thermal runaway and soot production of lithium-ion batteries: Implications for safety and environmental concerns. *Appl. Therm. Eng.* **2024**, *248*, 123193. [[CrossRef](#)]
26. Xu, Y.; Wang, Y.; Chen, D. Soot formation and its hazards in battery thermal runaway. *J. Aerosol Sci.* **2024**, *181*, 106420. [[CrossRef](#)]
27. ICRP. *Human Respiratory Tract Model for Radiological Protection, ICRP Publication 66*; International Commission on Radiological Protection (ICRP): Ottawa, ON, Canada, 1994; Volume 24, pp. 1–3.
28. Thangavel, P.; Park, D.; Lee, Y.C. Recent Insights into Particulate Matter (PM(2.5))-Mediated Toxicity in Humans: An Overview. *Int. J. Env. Res. Public Health* **2022**, *19*, 7511. [[CrossRef](#)]
29. Claassen, M.; Bingham, B.; Chow, J.C.; Watson, J.G.; Wang, Y.; Wang, X.L. Characterization of Lithium-ion Battery Fire Emissions—Part 2: Particle Size Distributions and Emission Factors. *Batteries*, **2024**; Submitted.
30. Lithiumwerks. APR18650M1B Nanophosphate® Technology Data Sheet. Austin, Texas. 2023. Available online: <https://lithiumwerks.com/products/lithium-ion-18650-cells/> (accessed on 1 February 2024).
31. AA Portable Power Corp. Model 544792 Polymer Lithium-Ion Battery Data Sheet; AA Portable Power Corp.: Richmond, CA, USA; Available online: <https://www.batteryspace.com/prod-specs/3175.pdf> (accessed on 1 February 2024).
32. Chombo, P.V.; Laoonual, Y. Prediction of the onset of thermal runaway and its thermal hazards in 18650 lithium-ion battery abused by external heating. *Fire Saf. J.* **2022**, *129*, 103560. [[CrossRef](#)]
33. Peng, P.; Jiang, F. Thermal safety of lithium-ion batteries with various cathode materials: A numerical study. *Int. J. Heat Mass Transf.* **2016**, *103*, 1008–1016. [[CrossRef](#)]
34. Nitta, N.; Wu, F.; Lee, J.T.; Yushin, G. Li-ion battery materials: Present and future. *Mater. Today* **2015**, *18*, 252–264. [[CrossRef](#)]
35. Barkholtz, H.M.; Preger, Y.; Ivanov, S.; Langendorf, J.; Torres-Castro, L.; Lamb, J.; Chalamala, B.; Ferreira, S.R. Multi-scale thermal stability study of commercial lithium-ion batteries as a function of cathode chemistry and state-of-charge. *J. Power Sources* **2019**, *435*, 226777. [[CrossRef](#)]
36. Anand, M.D.; Sasidharakurup, R.; Mercy, T.; Jacob, T.M.; Devi, S.A. Lithium-ion cells for space applications: Aspects of durability. *Adv. Space Res.* **2023**, *72*, 2948–2958. [[CrossRef](#)]

37. Dalton, P.J.; Schwanbeck, E.; North, T.; Balcer, S. International Space Station Lithium-Ion Battery. In Proceedings of the NASA Aerospace Battery Workshop, Huntsville, AL, USA, 15–17 November 2016.
38. Tian, J.; Chow, J.C.; Cao, J.; Han, Y.; Ni, H.; Chen, L.-W.A.; Wang, X.; Huang, R.; Moosmu, H.; Watson, J.G. A biomass combustion chamber: Design, evaluation, and a case study of wheat straw combustion emission tests. *Aerosol Air Qual. Res.* **2015**, *15*, 2104–2114. [CrossRef]
39. Goupil, V.; Gaya, C.; Boisard, A.; Robert, E. Effect of the heating rate on the degassing and combustion of cylindrical Li-Ion cells. *Fire Saf. J.* **2022**, *133*, 103648. [CrossRef]
40. Wang, X.L.; Zhou, H.; Arnott, W.P.; Meyer, M.E.; Taylor, S.; Firouzkouhi, H.; Moosmüller, H.; Chow, J.C.; Watson, J.G. Characterization of smoke for spacecraft fire safety. *J. Aerosol Sci.* **2019**, *136*, 36–47. [CrossRef]
41. Wang, X.L.; Firouzkouhi, H.; Chow, J.C.; Watson, J.G.; Carter, W.; De Vos, A.S. Characterization of gas and particle emissions from open burning of household solid waste from South Africa. *Atmos. Chem. Phys.* **2023**, *23*, 8921–8937. [CrossRef]
42. Wang, X.L.; Zhou, H.; Arnott, W.P.; Meyer, M.E.; Taylor, S.; Firouzkouhi, H.; Moosmüller, H.; Chow, J.C.; Watson, J.G. Evaluation of gas and particle sensors for detecting spacecraft-relevant fire emissions. *Fire Saf. J.* **2020**, *113*, 102977. [CrossRef]
43. Wang, X.L.; Chancellor, G.; Evenstad, J.; Farnsworth, J.E.; Hase, A.; Olson, G.M.; Sreenath, A.; Agarwal, J.K. A Novel Optical Instrument for Estimating Size Segregated Aerosol Mass Concentration in Real Time. *Aerosol Sci. Technol.* **2009**, *43*, 939–950. [CrossRef]
44. Järvinen, A.; Aitomaa, M.; Rostedt, A.; Keskinen, J.; Yli-Ojanperä, J. Calibration of the new electrical low pressure impactor (ELPI+). *J. Aerosol Sci.* **2014**, *69*, 150–159. [CrossRef]
45. Saari, S.; Arffman, A.; Harra, J.; Rönkkö, T.; Keskinen, J. Performance evaluation of the HR-ELPI+ inversion. *Aerosol Sci. Technol.* **2018**, *52*, 1037–1047. [CrossRef]
46. Wang, X.; Firouzkouhi, H.; Chow, J.C.; Watson, J.G.; Ho, S.S.H.; Carter, W.; De Vos, A.S. Chemically speciated air pollutant emissions from open burning of household solid waste from South Africa. *Atmos. Chem. Phys.* **2023**, *23*, 15375–15393. [CrossRef]
47. Watson, J.G.; Tropp, R.J.; Kohl, S.D.; Wang, X.L.; Chow, J.C. Filter processing and gravimetric analysis for suspended particulate matter samples. *Aerosol Sci. Eng.* **2017**, *1*, 193–205. [CrossRef]
48. Watson, J.G.; Chow, J.C.; Frazier, C.A. X-ray fluorescence analysis of ambient air samples. In *Elemental Analysis of Airborne Particles*; Landsberger, S., Creatchman, M., Eds.; Gordon and Breach Science: Amsterdam, The Netherlands, 1999; Volume 1, pp. 67–96.
49. Chow, J.C.; Watson, J.G. Enhanced Ion Chromatographic Speciation of Water-Soluble PM_{2.5} to Improve Aerosol Source Apportionment. *Aerosol Sci. Eng.* **2017**, *1*, 7–24. [CrossRef]
50. Chow, J.C.; Watson, J.G.; Chen, L.-W.A.; Chang, M.C.O.; Robinson, N.F.; Trimble, D.; Kohl, S. The IMPROVE_A temperature protocol for thermal/optical carbon analysis: Maintaining consistency with a long-term database. *J. Air Waste Manag. Assoc.* **2007**, *57*, 1014–1023. [CrossRef]
51. Chen, L.-W.A.; Chow, J.C.; Wang, X.L.; Robles, J.A.; Sumlin, B.; Lowenthal, D.H.; Zimmermann, R.; Watson, J.G. Multi-wavelength optical measurement to enhance thermal/optical analysis for carbonaceous aerosol. *Atmos. Meas. Tech.* **2015**, *8*, 451–461. [CrossRef]
52. Chow, J.C.; Wang, X.L.; Sumlin, B.J.; Gronstal, S.B.; Chen, L.-W.A.; Hurbain, M.J.; Zimmermann, R.; Watson, J.G. Optical Calibration and Equivalence of a Multiwavelength Thermal/Optical Carbon Analyzer. *Aerosol Air Qual. Res.* **2015**, *15*, 1145–1159. [CrossRef]
53. Watson, J.G.; Turpin, B.J.; Chow, J.C. The measurement process: Precision, accuracy, and validity. In *Air Sampling Instruments for Evaluation of Atmospheric Contaminants*, 9th ed.; Cohen, B.S., McCammon, C.S., Jr., Eds.; American Conference of Governmental Industrial Hygienists: Cincinnati, OH, USA, 2001; pp. 201–216.
54. Wang, X.; Chow, J.C.; Kohl, S.D.; Percy, K.E.; Legge, A.H.; Watson, J.G. Characterization of PM_{2.5} and PM₁₀ fugitive dust source profiles in the Athabasca Oil Sands Region. *J. Air Waste Manag. Assoc.* **2015**, *65*, 1421–1433. [CrossRef] [PubMed]
55. Chow, J.C.; Lowenthal, D.H.; Chen, L.-W.A.; Wang, X.L.; Watson, J.G. Mass reconstruction methods for PM_{2.5}: A review. *Air Qual. Atmos. Health* **2015**, *8*, 243–263. [CrossRef]
56. Wang, X.; Gronstal, S.; Lopez, B.; Jung, H.; Chen, L.-W.A.; Wu, G.; Ho, S.S.H.; Chow, J.C.; Watson, J.G.; Yao, Q. Evidence of non-tailpipe emission contributions to PM_{2.5} and PM₁₀ near southern California highways. *Environ. Pollut.* **2023**, *317*, 120691. [CrossRef]
57. U.S. EPA. *Quality Assurance Guidance Document—Quality Assurance Project Plan: PM_{2.5} Chemical Speciation Sampling at Trends, NCORE, Supplemental and Tribal Sites*; Ambient Air Monitoring Group, Air Quality Assessment Division, US EPA, Office of Air Quality Planning and Standards: Research Triangle Park, NC, USA, 2012. Available online: https://www3.epa.gov/ttnamt1/files/ambient/pm25/spec/CSN_QAPP_v120_05-2012.pdf (accessed on 26 June 2024).
58. Chow, J.C.; Watson, J.G.; Crow, D.; Lowenthal, D.H.; Merrifield, T. Comparison of IMPROVE and NIOSH Carbon Measurements. *Aerosol Sci. Technol.* **2001**, *34*, 23–34. [CrossRef]
59. Zhang, Y.; Wang, H.; Li, W.; Li, C. Quantitative identification of emissions from abused prismatic Ni-rich lithium-ion batteries. *eTransportation* **2019**, *2*, 100031. [CrossRef]
60. Yang, Y.; Fang, D.; Maleki, A.; Kohzadi, S.; Liu, Y.; Chen, Y.; Liu, R.; Gao, G.; Zhi, J. Characterization of Thermal-Runaway Particles from Lithium Nickel Manganese Cobalt Oxide Batteries and Their Biotoxicity Analysis. *ACS Appl. Energy Mater.* **2021**, *4*, 10713–10720. [CrossRef]

61. Bordes, A.; Marlair, G.; Zantman, A.; Herreyre, S.; Papin, A.; Desprez, P.; Lecocq, A. New insight on the risk profile pertaining to lithium-ion batteries under thermal runaway as affected by system modularity and subsequent oxidation regime. *J. Energy Storage* **2022**, *52*, 104790. [[CrossRef](#)]
62. Wang, H.; Zhang, Y.; Li, W.; Li, C.; Ouyang, M. Particles released by abused prismatic Ni-rich automotive lithium-ion batteries. *WSEAS Trans. Syst. Control* **2020**, *15*, 30–38. [[CrossRef](#)]
63. Krebs, R.; Owens, J.; Luckarift, H. Formation and detection of hydrogen fluoride gas during fire fighting scenarios. *Fire Saf. J.* **2022**, *127*, 103489. [[CrossRef](#)]
64. Yuan, S.; Chang, C.; Yan, S.; Zhou, P.; Qian, X.; Yuan, M.; Liu, K. A review of fire-extinguishing agent on suppressing lithium-ion batteries fire. *J. Energy Chem.* **2021**, *62*, 262–280. [[CrossRef](#)]
65. Saldaña, G.; San Martín, J.I.; Zamora, I.; Asensio, F.J.; Oñederra, O. Analysis of the current electric battery models for electric vehicle simulation. *Energies* **2019**, *12*, 2750. [[CrossRef](#)]
66. Chow, J.C.; Watson, J.G.; Chen, L.-W.A.; Rice, J.; Frank, N.H. Quantification of PM2.5 organic carbon sampling artifacts in US networks. *Atmos. Chem. Phys.* **2010**, *10*, 5223–5239. [[CrossRef](#)]

Disclaimer/Publisher's Note: The statements, opinions and data contained in all publications are solely those of the individual author(s) and contributor(s) and not of MDPI and/or the editor(s). MDPI and/or the editor(s) disclaim responsibility for any injury to people or property resulting from any ideas, methods, instructions or products referred to in the content.